



Article

Influences of Plasma Plume Length on Structural, Optical and Dye Degradation Properties of Citrate-Stabilized Silver Nanoparticles Synthesized by Plasma-Assisted Reduction

Tirtha Raj Acharya ^{1,2} , Geon Joon Lee ^{1,2,*} and Eun Ha Choi ^{1,2,*}

¹ Department of Electrical and Biological Physics, Kwangwoon University, Seoul 01897, Korea; tirtharajacharya2050@gmail.com

² Plasma Bioscience Research Center, Kwangwoon University, Seoul 01897, Korea

* Correspondence: gjlee@kw.ac.kr (G.J.L.); ehchoi@kw.ac.kr (E.H.C.); Tel.: +82-2-940-8619 (G.J.L.); +82-2-940-5014 (E.H.C.)

Abstract: Citrate-capped silver nanoparticles *Ag@Cit NPs* were synthesized by a simple plasma-assisted reduction method. Homogenous colloidal *Ag@Cit NPs* solutions were produced by treating a AgNO_3 -trisodium citrate-deionized water with an atmospheric-pressure argon plasma jet. The plasma-synthesized *Ag@Cit NPs* exhibited quasi-spherical shape with an average particle diameter of about 5.9–7.5 nm, and their absorption spectra showed surface plasmon resonance peaks at approximately 406 nm. The amount of *Ag@Cit NPs* increased in a plasma exposure duration-dependent manner. Plasma synthesis of *Ag@Cit NPs* was more effective in the 8.5 cm plume jet than in the shorter and longer plume jets. A larger amount of *Ag@Cit NPs* were produced from the 8.5 cm plume jet with a higher pH and a larger number of aqua electrons, indicating that the synergetic effect between plasma electrons and citrate plays an important role in the plasma synthesis of *Ag@Cit NPs*. Plasma-assisted citrate reduction facilitates the synthesis of *Ag@Cit NPs*, and citrate-capped nanoparticles are stabilized in an aqueous solution due to their repulsive force. Next, we demonstrated that plasma-synthesized *Ag@Cit NPs* exhibited a significant degradation of methylene blue dye.

Keywords: silver nanoparticles; plasmon; plasma synthesis; plasma-treated water; reactive oxygen species; citrate



Citation: Acharya, T.R.; Lee, G.J.; Choi, E.H. Influences of Plasma Plume Length on Structural, Optical and Dye Degradation Properties of Citrate-Stabilized Silver Nanoparticles Synthesized by Plasma-Assisted Reduction. *Nanomaterials* **2022**, *12*, 2367. <https://doi.org/10.3390/nano12142367>

Academic Editor: Lei Shao

Received: 2 June 2022

Accepted: 6 July 2022

Published: 11 July 2022

Publisher's Note: MDPI stays neutral with regard to jurisdictional claims in published maps and institutional affiliations.



Copyright: © 2022 by the authors. Licensee MDPI, Basel, Switzerland. This article is an open access article distributed under the terms and conditions of the Creative Commons Attribution (CC BY) license (<https://creativecommons.org/licenses/by/4.0/>).

1. Introduction

Metal nanoparticles have interesting physical, electrical, optical, and antimicrobial characteristics that make them useful in various fields, including biomedicine, healthcare, food storage, textiles, agriculture, catalysis, optical sensors, flexible electronics, solar cells, drug delivery, cosmetics, antimicrobial action, chemical sensing, and environmental engineering [1–3]. Silver nanoparticles (*AgNPs*) can be fabricated by various methods, such as thermal evaporation [4], plasma synthesis [5–7], microwave-assisted synthesis [8], gamma ray-assisted synthesis [9], spray pyrolysis [10], laser ablation [11], citrate reduction [12–14], and electrochemical synthesis [15]. Among these synthesis routes, the chemical reduction method has been widely used due to its advantages of simplicity, high yield, no aggregation, and low cost [7,12,13]. To create silver nanoparticles, it is necessary to add chemical reducing agents to silver salt ions and reduce silver ions in boiling water. In addition, stabilizers such as citrate [16], polyvinyl alcohol [17], polyvinyl pyrrolidone [6], bovine serum albumin [18], and cellulose [19] are extensively used to avoid aggregation of nanoparticles.

Recently, atmospheric-pressure plasma jets have received a lot of interest as a promising green means for the synthesis of nanomaterials [5,20]. Metallic nanoparticles can be produced by applying atmospheric-pressure plasma jets [5,20], dielectric barrier discharge plasma [21], gas–liquid interfacial plasmas [22], and dual plasma electrolysis [23] to aqueous metal salt solutions. Among these plasma synthesis methods, metal nanoparticle

synthesis with atmospheric-pressure plasma jets is relatively simple, cost-effective, and efficient. Interestingly, plasma synthesis of metal nanoparticles can be carried out in a shorter processing time as compared with their synthesis by the chemical reduction method. Furthermore, the plasma jets can synthesize metal nanoparticles in an atmospheric environment without vacuum devices, and can be operated using various gases. Noble gases such as argon, helium, and neon are easily ionized as compared to air [24]. In this research, argon gas was used as the plasma working gas. Argon is the cheapest noble gas. The Ar plasma jets are simple, affordable, and easy to design. The plasma jets can produce reactive oxygen and nitrogen species, charged particles, ultraviolet (UV) light, and electric fields. When the plasma jet enters the deionized water (DW), additional reactive species are generated by plasma–liquid interactions [25–27]. If the plasma jet is applied to an aqueous metal salt solution, plasma-generated reactive species will be affected by the reducing and scavenging activities of the plasma-activated medium [5,25,26]. Plasma-assisted reduction of metal ions can be employed for the synthesis of various metal nanoparticles, such as Ag, Au, Cu, Fe, and alloy nanoparticles [5,20,28]. In the plasma-assisted reduction of metal ions, plasma-induced reactive species determine key parameters affecting the synthesis of metal nanoparticles. The amount of plasma-synthesized metal nanoparticles depends on the aqua electron density and the acidity of the plasma-activated medium [5,24]. Kondeti et al. synthesized silver nanoparticles using a hydrogen plasma jet [5], and Lee et al. produced silver nanoparticles using liquid phase plasma [7]. However, no systematic study has been performed on the plasma synthesis mechanism of silver nanoparticles by atmospheric-pressure argon plasma jets and the influence of plasma plume length on the structural and optical properties of plasma-synthesized silver nanoparticles.

In this research, we used the plasma-assisted reduction method to synthesize citrate-stabilized silver nanoparticles (*Ag@Cit NPs*). An atmospheric-pressure argon plasma jet was used for plasma synthesis of *Ag@Cit NPs* in a single-step approach. Trisodium citrate (TSC) was used to stabilize *AgNPs* and to enhance the plasma synthesis efficiency. To diagnose the plasma, key plasma parameters such as current–voltage waveforms of plasma discharge, electron density, electron temperature, and optical emission spectra of the plasma plume, were measured. To study the effects of plasma treatment on DW and AgNO_3 -TSC-DW, their acidity and electrical conductivity were measured. To analyze the structural and optical properties of plasma-synthesized *Ag@Cit NPs*, their transmission electron microscopy (TEM) images and optical absorption spectra were examined. To identify plasma synthesis routes of *Ag@Cit NPs*, the effects of plasma treatment duration and plasma plume lengths on plasma-synthesized *Ag@Cit NPs* were investigated. To demonstrate applications of plasma-synthesized *Ag@Cit NPs*, the degradation effects of plasma-synthesized *Ag@Cit NPs* on methylene blue (MB) dye were measured.

2. Experimental Methods

2.1. Characteristics of the Plasma Device

In this research, an alternating current (AC)-driven argon plasma jet (Figure 1) was used for synthesis of *Ag@Cit NPs*. The plasma device consists of a powered needle electrode and a grounded copper tape electrode. A stainless-steel needle electrode (with a length of 50 mm, an inner diameter of 0.6 mm, and an outer diameter of 0.9 mm) was used as the power electrode. For grounding, a copper tape was fixed to the bottom of a glass beaker that contained AgNO_3 -TSC-DW. A plasma jet was created from a needle electrode inserted inside a quartz tube (with an inner diameter of 2 mm and an outer diameter of 4 mm). Argon gas entered the quartz tube through a needle, and was supplied to the needle with a gas flow rate of 500 standard cubic centimeters per minute (sccm). As plasma can propagate a long distance along an argon gas stream in a quartz tube, plasma plume length is longer for a longer quartz tube [29]. Three different plasma jets with plume lengths of 2.5, 8.5, and 12.5 cm were used to study the effect of plasma plume length on the synthesis of *Ag@Cit NPs*. To make plasma jets with plume lengths of 2.5, 8.5, and 12.5 cm, a powered needle electrode was inserted inside each of 6.5, 11.5, and 15.5 cm long quartz

tubes (Figure 1b). In this research, plasma jets with plume lengths of 2.5, 8.5, and 12.5 cm are called J1, J2, and J3 jets, respectively, (Figure 1c). When the plasma jet exited the nozzle of the quartz tube, the plasma plume region was at a lower pressure than the surrounding ambient air. Thus, the ambient air diffused into and directly mixed with the plasma plume below the nozzle of the quartz tube. Due to the quenching effect of atmospheric air, the plasma plume was weakened after traveling a few centimeters away from the nozzle of the quartz tube. The plasma plume lengths of J1, J2, and J3 jets were longer than their needle-to-nozzle distances. After the plasma jet exited the nozzle of the quartz tube, it propagated a few centimeters away from the nozzle. In Figure 1c, the purple color at the end of the plasma plume was due to the nitrogen emission obtained from the diffused air. After nitrogen emission, the plasma plume dissipated. In this research, the plasma jet entered the aqueous silver salt solution, and the penetration depth of the plasma plume from the water surface was adjusted to be approximately 5 mm. As the plasma plume was charged and the end of it was in contact with the water–air interface, the electric field was applied to aqua electrons and silver ions in the solutions.

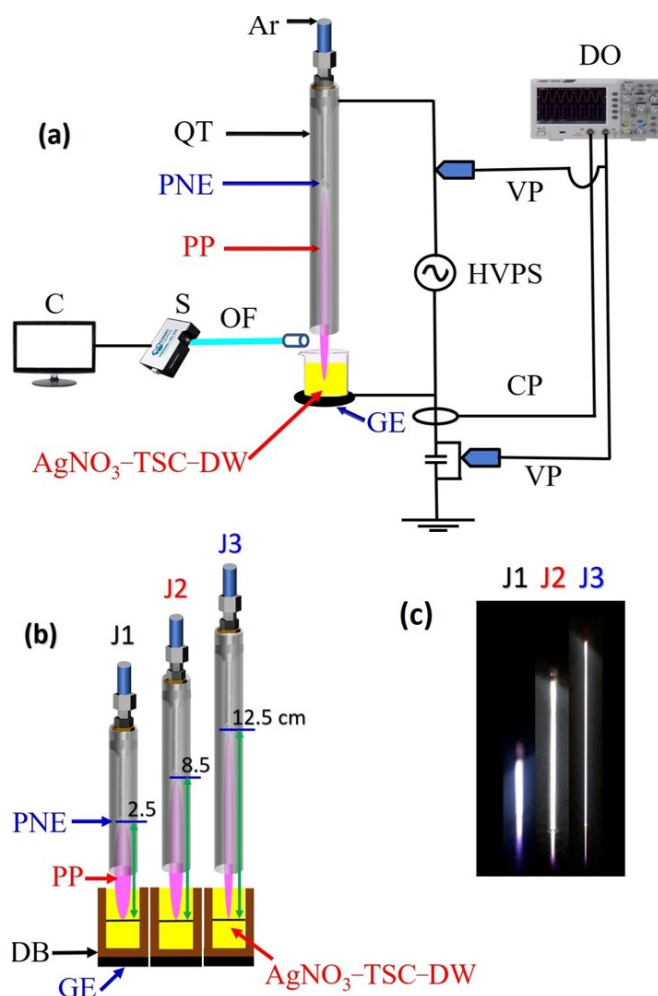


Figure 1. (a) Experimental layout of a plasma jet device for synthesis of silver nanoparticles; (b) schematic diagram; (c) photos of the J1, J2, and J3 jets. In (a,b), Ar, argon gas; QT, quartz tube; PNE, powered needle electrode; PP, plasma plume; OF, optical fiber; S, spectrometer; C, computer; DB, dielectric barrier; GE, grounded electrode; $\text{AgNO}_3\text{-TSC-DW}$, $\text{AgNO}_3\text{-TSC-DW}$ solution for synthesis of silver nanoparticles; HVPS, high voltage power supply; VP, voltage probe; CP, Current probe; DO, digital oscilloscope.

To investigate the reactive oxygen and nitrogen species produced by the plasma jet, optical emission spectra were recorded by a fiber optic spectrometer (HR4000, Ocean

Optics, Orlando, FL, USA). Optical emission of the propagating plasma jet was collected near the water–air interface, as shown in Figure 1a. Meanwhile, Balmer emission of excited hydrogen atoms was measured in the end-on geometry to detect hydrogen produced in the AgNO_3 -TSC-DW by the plasma-liquid interactions. For this purpose, a copper tape with a circular hole was fixed to the bottom of a beaker that contained AgNO_3 -TSC-DW, and hydrogen emission was measured from the plasma light that transmitted through a hole of a copper electrode below the plasma-treated AgNO_3 -TSC-DW. To examine surface plasmon resonance effects, absorption spectra of plasma-synthesized $\text{Ag}@ \text{Cit}$ NPs were measured by an optical absorption spectrometer (Maya2000Pro, Ocean Insight, Orlando, FL, USA). The pH and electrical conductivity of the plasma-treated- AgNO_3 -TSC-DW were measured by pH and conductivity meters (PCTSTestrTM 50, Oakton, Melbourne, Australia).

2.2. Electrical Characteristics of Plasma Discharge

To measure the applied voltage and discharge current, a high-voltage probe (P6015A, Tektronix, Beaverton, OR, USA) and a current probe (CP030, LeCroy, Chestnut Ridge, NY, USA) were connected to a digital oscilloscope (WaveSurfer 434, Lecroy, New York, NY, USA). Figure 2a shows typical current and voltage waveforms of the AC-driven plasma discharge for the J2 jet. Several positive current peaks appeared with increasing applied voltage and resulted in accumulation of charges inside the quartz tube. The accumulation of positive surface charges in the positive half-cycle of the applied voltage caused discharge current peaks, and the polarity of these charges was reversed in the negative half-cycle of the applied voltage. The measured discharge currents of J1, J2, and J3 jets were 46, 43, and 34 mA, respectively, at a fixed peak voltage of 4.8 kV (rms). The current and voltage waveforms had a period of 31.5 μs , which corresponded to a frequency of 32 kHz. To determine the accumulated charge, we connected a 10 nF ceramic capacitor in series to the ground electrode and measured the voltage across it. The corresponding charge (Q)–voltage (V) Lissajous plot is shown in Figure 2b. The Q–V plot forms a closed loop, and its area represents the total energy dissipated in one cycle [30]. The dissipated powers of J1, J2, and J3 jets were measured to be 8.9, 8.5, and 4.0 W, respectively, corresponding to unit cycle energy dissipation of 0.28, 0.27, and 0.13 mJ.

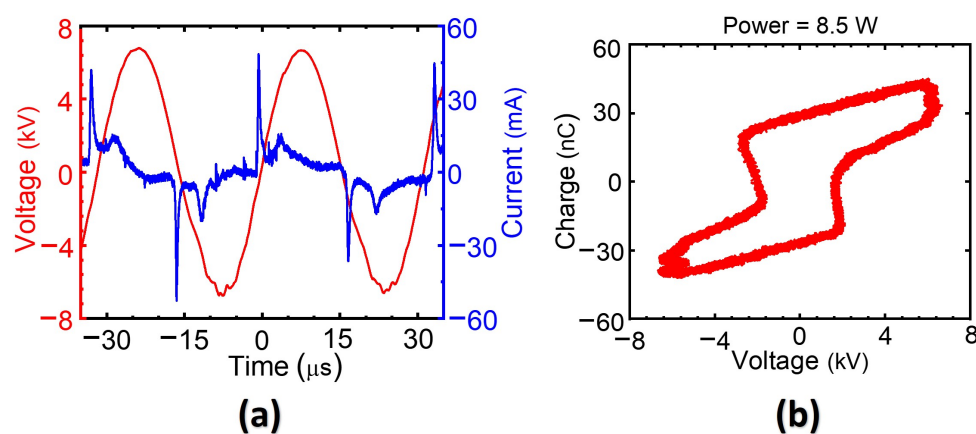


Figure 2. (a) Typical current and voltage waveforms of the plasma discharge for the J2 jet, and (b) corresponding Lissajous plot.

Electron temperature and density are key plasma parameters affecting the synthesis of metal nanoparticles [25,31,32]. Energy transfer from the thermally excited electrons to the ions increased due to the high electron densities in the discharged plasma, and the electron cooling rate was high. Higher electron densities typically imply lower electron temperatures, and vice versa. Long plasma jets feature more frequent elastic collisions between electrons and heavier particles than do shorter plasma jets. Consecutive energy impact collisions with heavy particles cooled the electron temperature of the long jet rather than

that of the short jet. Electron temperature and density also have an impact on the interaction between the plasma jet and the liquid medium [26,31]. In the plasma-assisted reduction of silver ions, the amount of plasma-synthesized silver nanoparticles depends on the electron density and acidity of plasma-activated medium. Electron temperatures and densities of the J1, J2, and J3 jets at the nozzle of the quartz tube are shown in Figure 3a,b. Electron temperatures of the J1, J2, and J3 jets were 1.38, 1.31, and 1.28 eV, respectively. Electron densities of J1, J2, and J3 jets were 0.45×10^{21} , 2.33×10^{21} , and 4.30×10^{21} electrons/m³, respectively. The collisional radiative model [33] and the convective wave packet model [34] were used to compute electron temperature and density, respectively.

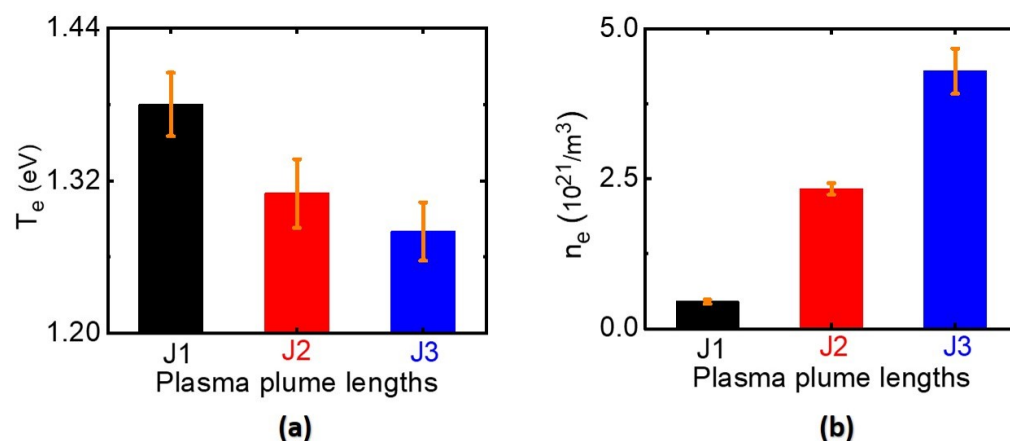


Figure 3. (a) Electron temperature and (b) electron density of the J1, J2, and J3 jets.

2.3. Plasma Synthesis of Silver Nanoparticles

Silver nitrate (AgNO_3) and trisodium citrate (TSC, $\text{Na}_3\text{C}_6\text{H}_5\text{O}_7$) were purchased from Sigma-Aldrich (Yongin-city, Kyunggi-do, Korea). Stock solutions of 25 mM AgNO_3 and 50 mM TSC were prepared. To synthesize Ag@Cit NPs, solutions of 4.0 mM AgNO_3 and 8.0 mM TSC ($\text{AgNO}_3\text{:TSC} = 1\text{:}2$) were prepared by mixing 4.8 mL of 25 mM AgNO_3 and 4.8 mL of 50 mM TSC with 20 mL DW, respectively. Then, 8 mL of the $\text{AgNO}_3\text{-TSC-DW}$ was treated by the atmospheric-pressure Ar plasma jet [5,16]. The plasma treatment durations were 2, 5, 7.5, and 10 min. To find the optimum conditions for plasma synthesis and to study plasma synthesis routes, we investigated the effects of plasma treatment duration and plasma plume length on the physical properties of plasma-synthesized Ag@Cit NPs.

2.4. Structural and Optical Characterizations of Plasma-Synthesized Silver Nanoparticles

To investigate the structural properties of plasma-synthesized Ag@Cit NPs, high-resolution transmission electron microscopy (HR-TEM) and EDS mapping were conducted using a Cs-corrected scanning transmission electron microscope (Neo ARM, JEOL, Tokyo, Japan). For measuring TEM images, the Ag@Cit NPs solution was drop-cast on a carbon-stabilized Formvar-coated 200 mesh copper TEM grid (Ted Pella #01801, Redding, CA, USA), and dried at room temperature under atmospheric conditions. The size distributions of plasma-synthesized AgNPs were obtained by analysis with ImageJ software, v1.53s (National Institutes of Health, Bethesda, MD, USA). To confirm the surface plasmon resonance effects, absorption spectra of plasma-synthesized Ag@Cit NPs were measured by an optical absorption spectrometer (Maya2000Pro, Ocean Insight, Orlando, FL, USA).

2.5. Measurements of Dye Degradation by Plasma-Synthesized Silver Nanoparticles

A nonbiodegradable and commonly used organic dye, methylene blue (MB), was selected as a model analyte. MB and sodium borohydride (NaBH_4) were purchased from Sigma-Aldrich (Yongin-city, Kyunggi-do, Korea). To investigate the degradation activity of MB dye by plasma-synthesized Ag@Cit NPs, 0.3 mL of 1 mM MB was mixed with 10 mL DW, 0.3 mL of 100 mM NaBH_4 , and 1.0 mL of Ag@Cit NPs. For the dye degradation

experiment, the plasma-synthesized *Ag@Cit NP* solutions were diluted 11.6-fold with DW. Consequently, solutions with 26 μM MB were treated by the plasma-synthesized *Ag@Cit NPs*. The *Ag@Cit NP* treatment duration was 10 min. Optical absorption spectra of *Ag@Cit NP*-treated and -untreated MB solutions were measured by an optical absorption spectrometer (Maya2000Pro, Ocean Insight, Orlando, FL, USA).

Next, we investigated dye degradation activity of plasma-synthesized *Ag@Cit NPs* coated onto filter paper to achieve dye degradation without remnant silver nanoparticles. The filter paper was immersed in a *Ag@Cit NP* solution for 3 h and dried at 60 °C for 1 h. After drying, most of the plasma-activated liquid was removed. In this research, *Ag@Cit NPs* loaded onto the filter paper is called *Ag@Cit NP-paper*. To examine dye degradation effects of the *Ag@Cit NP-paper*, *Ag@Cit NP*-coated and -uncoated papers were soaked in 26 μM MB solutions. After dye degradation treatment for 1 h in the *Ag@Cit NP-paper*-containing solution, pristine and *Ag@Cit NP-paper*-treated MB solutions were transferred into a 15 mL conical tube and used for further experiments.

3. Results and Discussion

3.1. Optical Properties of the Plasma Jet

Optical emission spectroscopy is a common, fast, simple, and straightforward method to investigate the various reactive and energized species in the plasma jet. Optical emission spectra (OES) of the J1, J2, and J3 jets in the 200–1000 nm region displayed the characteristic emission peaks of plasma-induced reactive oxygen and nitrogen species, as shown in Figure 4a. The emission lines in the 700–900 nm region are attributed to $2p \rightarrow 1s$ transition of excited argon molecules [35]. Intense emission at 309 nm corresponds to the hydroxyl radical (OH) produced by breakdown of water molecules present in ambient air under the influence of electrons and metastable atoms [36,37]. At the plasma–liquid interface, prolonged plasma exposure causes a dissociation of water molecules by energetic ions from the plasma jet, resulting in OH radical generation. Weak emission bands in the 330–380 nm range are generated from the second positive system transition of nitrogen molecules ($\text{C}^3\Pi_u \rightarrow \text{B}^3\Pi_g$) [37,38], which can be ascribed to plasma operation under atmospheric conditions. The emission at 777 nm was attributed to $2s^22p^3(^4S^0)3s \rightarrow 2s^22p^3(^4S^0)3p$ transition of atomic oxygen (O) [39]. The emission line at 656 nm was attributed to Balmer H_α transition of excited hydrogen atoms (Figure 4b). The Balmer emission indicates that hydrogen atoms were produced in the AgNO_3 -TSC-DW. Under our experimental conditions, most of the hydrogen atoms were produced from the plasma electron reduction of hydrogen ions that came from citrate (TSC). As shown in Figure 4b, the hydrogen emission intensity was stronger in the J2 and J3 jets than the J1 jet, which was attributed to the higher concentration of plasma electrons in the longer jet. Meanwhile, the hydrogen emission intensity of the J3 jet was lower than the expectation from the plasma electron-induced reduction of hydrogen ions. The hydrogen emission intensity of the J3 jet was slightly higher than that of the J2 jet. Hydrogen generation by plasma electron reduction of hydrogen ions may compete with other product generation processes by reaction of hydrogen atoms with plasma-induced reactive species (hydroxyl radical, hydroperoxyl radical, etc.). Next, the J1 jet produced more reactive nitrogen species (RNS) than the longer jet (Figure 4a). Only a small fraction of nitrogen molecules can be dissociated in the outflow of the longer jet due to the lower electron temperature. Electron excitation and ionization of nitrogen molecules are more favorable in the J1 jet because the shorter jet exhibited a higher electron temperature than the longer jet (Figure 3). The binding of plasma-induced nitrate (nitrite) with hydrogen ions led to acidic water and prevents H^+ -to-H conversion, leading to the suppression of the plasma synthesis of *AgNPs* in the J1 jet. Overall, the longer jet generated a larger number of hydrogen atoms and a smaller amount of RNS in the AgNO_3 -TSC-DW.

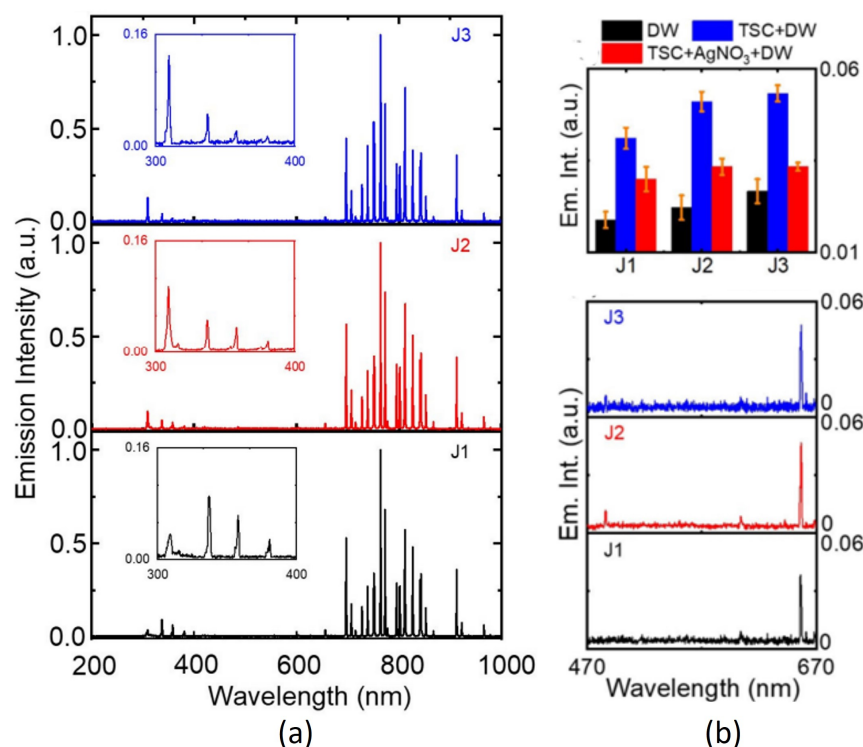


Figure 4. (a) Optical emission spectra of the J1, J2, and J3 jets in the 200–1000 nm range. The 309 nm and 330–380 nm emission bands correspond to the hydroxyl radical and the second positive system transition of nitrogen molecules, respectively. (b) (**top**) Hydrogen emission intensities of DW, TSC-DW, and AgNO₃-TSC-DW treated for 10 min with the J1, J2, and J3 jets. (**bottom**) Hydrogen emission spectra of AgNO₃-TSC-DW treated for 10 min with the J1, J2, and J3 jets.

3.2. Electrical Conductivity and Acidity of Plasma-Treated Silver Precursor Solutions

Electrical conductivity and pH are key parameters governing the physicochemical properties of a plasma-activated medium. Atmospheric-pressure plasma in contact with an aqueous solution produces aqua electrons, resulting in the transport of electrons from the gaseous plasma into the aqueous solution [40,41]. Aqua electrons can affect the electrical conductivity and acidity of plasma-treated silver precursor solutions. To study the plasma synthesis mechanism of AgNPs, we measured the conductivities and pH values of plasma-treated silver precursor solutions. As shown in Figure 5, the electrical conductivities of the plasma-treated-DW and AgNO₃-TSC-DW increased significantly with plasma treatment duration. When DW was treated with the plasma jet for 10 min, the electrical conductivities of plasma-treated-DW rose from 0 $\mu\text{S}/\text{cm}$ to 63, 99, and 107 $\mu\text{S}/\text{cm}$ for the J1, J2, and J3 jets, respectively (Figure 5a). The electrical conductivities of plasma-treated AgNO₃-TSC-DW jumped from 970 $\mu\text{S}/\text{cm}$ to 1044, 1085, and 1093 $\mu\text{S}/\text{cm}$ for the J1, J2, and J3 jets, respectively, (Figure 5b). The plasma-untreated AgNO₃-TSC-DW showed electrical conductivity of 970 $\mu\text{S}/\text{cm}$. During plasma treatment, plasma-generated aqua electrons accumulated in the plasma-treated AgNO₃-TSC-DW. As shown in Figure 5c, AgNO₃ and TSC contribute to the electrical conductivity of the AgNO₃-TSC-DW. Plasma treatment for AgNO₃-DW, TSC-DW, and AgNO₃-TSC-DW increased their electrical conductivities due to plasma-generated aqua electrons. By subtracting the electrical conductivity of plasma-untreated AgNO₃-TSC-DW (σ_c) from the electrical conductivity of the plasma-treated AgNO₃-TSC-DW (σ_p), we obtained the electrical conductivity of plasma-generated aqua electrons ($\sigma_{e(aq)} = \sigma_p - \sigma_c$). For a plasma treatment duration of 10 min, the electrical conductivities of plasma-generated aqua electrons were estimated to be 74, 115, and 123 $\mu\text{S}/\text{cm}$ for the J1, J2, and J3 jets, respectively, as shown in Figure 6. The concentration of plasma-induced aqua electrons can be estimated from their electrical conductivity:

$n_{e(aq)} = \sigma_{e(aq)} / (e \cdot \mu_e)$. Here, $n_{e(aq)}$, e , and μ_e are the concentration, charge, and mobility of aqua electrons in the plasma-treated-AgNO₃-TSC-DW, respectively. From the reported value ($\mu_e = 1.84 \times 10^{-3} \text{ cm}^2 / (\text{V} \cdot \text{s})$) for the mobility of aqua electrons [42], we can estimate the aqua electron density of plasma-activated medium. For a plasma treatment duration of 10 min, the aqua electron densities of plasma-treated AgNO₃-TSC-DW increased to $2.5 \times 10^{21} / \text{m}^3$, $3.9 \times 10^{21} / \text{m}^3$, and $4.2 \times 10^{21} / \text{m}^3$ for the J1, J2 and J3 jets, respectively, as shown in Figure 6. The aqua electron density of the longer jet was higher than that of the shorter jet.

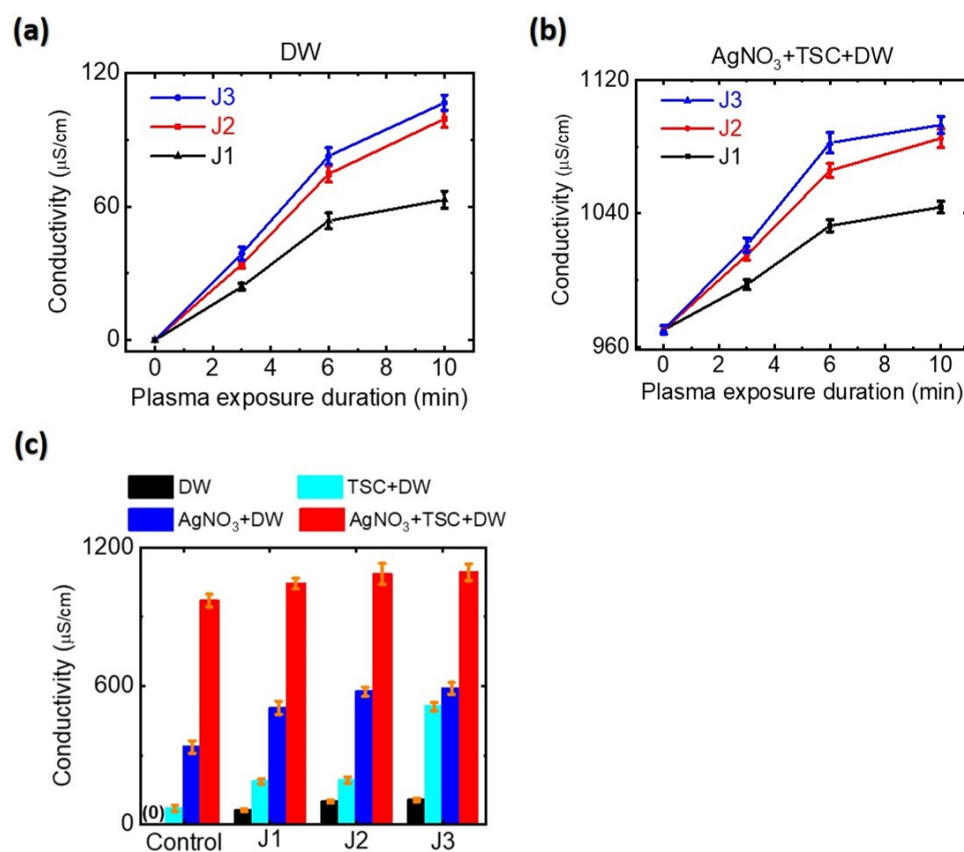


Figure 5. Electrical conductivities of (a) plasma-treated-DW and (b) plasma-treated AgNO₃-TSC-DW as a function of plasma exposure duration. (c) Electrical conductivities of DW, TSC-DW, AgNO₃-DW, and AgNO₃-TSC-DW treated for 10 min with the J1, J2, and J3 jets. In Figure (c), the electrical conductivity of plasma-untreated DW was 0 $\mu\text{S/cm}$.

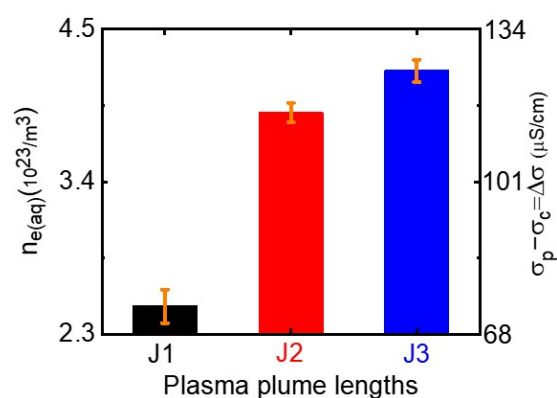


Figure 6. Aqua electron densities of plasma-treated AgNO₃-TSC-DW treated for 10 min with the J1, J2, and J3 jets.

When DW was treated for 10 min with the plasma jets, the pH values of plasma-treated-DW dropped from 7.0 to 4.5, 4.7, and 5.0 for the J1, J2, and J3 jets, respectively, as shown in Figure 7a. Prolonged plasma treatment of DW produced a lower pH. Plasma treatment of DW produced acidic water due to the plasma-induced hydrogen ion–nitrate (nitrite) complex formation. When TSC-DW was treated with the plasma jets for 10 min, the pH values of plasma-treated-TSC-DW were 6.8, 7.1, and 7.2 for the J1, J2, and J3 jets, respectively, (Figure 7c). The pH values of plasma-treated-TSC-DW are higher than those of plasma-treated-DW, indicating that TSC can scavenge plasma-generated hydrogen ions. For a plasma exposure duration of 10 min, the pH values of plasma-treated AgNO_3 -TSC-DW increased slightly to 7.3 to 7.5, 7.9, and 7.6 for the J1, J2, and J3 jets, respectively (Figure 7b). As described in the following section, plasma-assisted citrate reduction of silver ions can be facilitated at higher pH values.

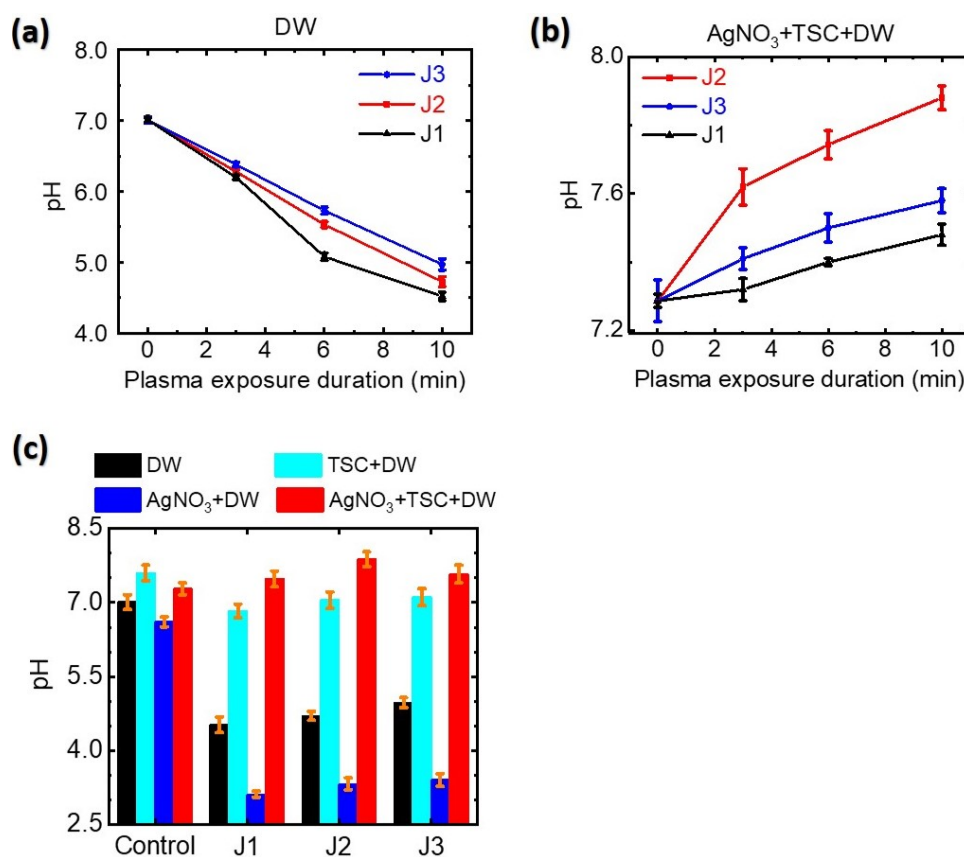


Figure 7. pH values of (a) plasma-treated-DW and (b) plasma-treated AgNO_3 -TSC-DW as a function of plasma exposure duration. (c) pH values of DW, TSC-DW, AgNO_3 -DW, and AgNO_3 -TSC-DW treated for 10 min with the J1, J2, and J3 jets.

3.3. Structural and Optical Properties of Plasma-Synthesized Silver Nanoparticles

After the AgNO_3 -TSC-DW was treated with the plasma jet for a few minutes, the color of the silver precursor solutions changed from colorless to yellow (Figure 8b), indicating that Ag@Cit NPs were successfully generated by plasma-assisted citrate reduction. Absorption spectra of the plasma-synthesized Ag@Cit NPs exhibited surface plasmon resonance (SPR) bands at approximately 406 nm (Figure 8a). As the plasma treatment duration increased from 2 min to 10 min, absorption coefficients of Ag@Cit NP solutions at the SPR peaks increased from 0.67/cm, 1.2/cm, and 0.75/cm to 4.0/cm, 8.6/cm, and 5.8/cm for the J1, J2 and J3 jets, respectively, (Figure 8c), indicating that prolonged plasma treatment produced a larger amount of Ag@Cit NPs. This happened because prolonged plasma treatment of silver precursor solutions led to more plasma reductants to be used for synthesis of Ag@Cit NPs. Regarding the effect of plasma plume length on the synthesis of Ag@Cit NPs, the SPR peak

intensity of *Ag@Cit* NPs was stronger in the J2 jet than the J1 and J3 jets, indicating that the J2 jet can synthesize a larger amount of *Ag@Cit* NPs than the shorter and longer jets. For a plasma treatment duration of 10 min, the SPR wavelengths of *Ag@Cit* NPs were 405.9, 405.0, and 406.9 nm for the J1, J2, and J3 jets, respectively, indicating similar average particle sizes of plasma-synthesized *Ag@Cit* NPs. This is because TSC stabilizes *Ag@Cit* NPs in an aqueous solution by suppressing their growth.

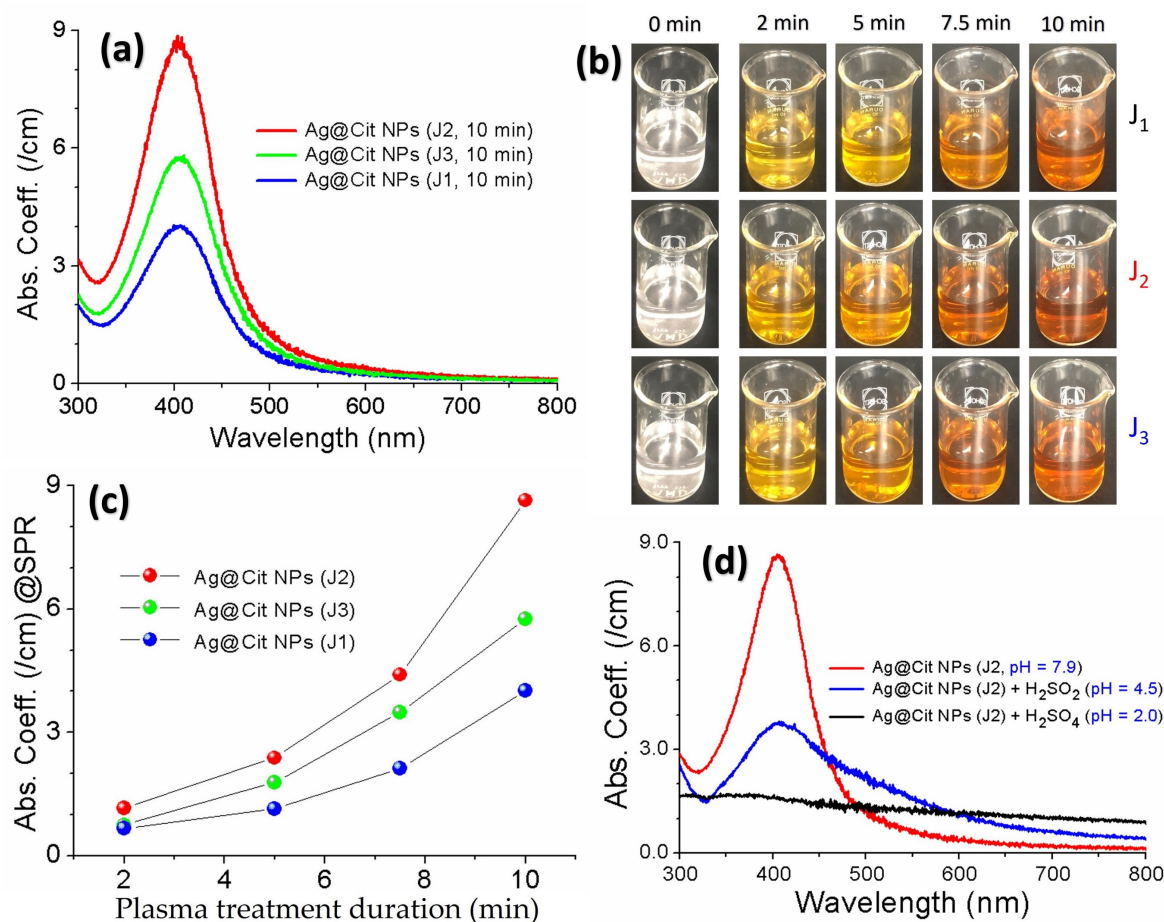


Figure 8. (a) Optical absorption spectra of the *Ag@Cit* NPs synthesized by treating AgNO_3 -TSC-DW for 10 min with the J1, J2, and J3 jets. (b) Color change of the plasma-synthesized *Ag@Cit* NPs over the plasma treatment durations of 2, 5, 7.5, and 10 min. (c) SPR peak intensity of the *Ag@Cit* NPs as a function of the plasma treatment duration. (d) Effects of acid treatments on the surface plasmon resonance absorption band of the *Ag@Cit* NPs synthesized with the J2 jet: H_2SO_4 (pH = 2) and H_2SO_4 (pH = 4.5).

Figure 9a shows the HR-TEM images of the *Ag@Cit* NPs synthesized by treating AgNO_3 -TSC-DW for 10 min with the J1, J2, and J3 jets. The *Ag@Cit* NPs by the J2 jet exhibited a single size distribution that could fit to Gaussian and Lorentzian functions, but the *Ag@Cit* NPs by the J1 and J3 jets caused two size distributions: one smaller and one larger. Considering that the *Ag@Cit* NPs by the J1, J2, and J3 jets exhibited a single SPR peak at approximately 406 nm, larger nanoparticles might be produced from the aggregation of nanoparticles during the drop casting of nanoparticles on the TEM grid. In the HR-TEM images of the *Ag@Cit* NPs by the J1 and J3 jets, smaller nanoparticles correspond to plasma-synthesized *Ag@Cit* NPs. Plasma-synthesized *Ag@Cit* NPs featured a quasi-spherical shape with average particle diameters of 7.5 ± 2.1 , 6.6 ± 2.0 , and 5.9 ± 2.1 nm for the J1, J2, and J3 jets, respectively, (Figure 9b). Figure 9c shows the electron diffraction patterns of the dense *Ag@Cit* NPs. The electron diffraction patterns of the *Ag@Cit* NPs are consistent with the {111}, {200}, {220}, and {311} crystallographic planes of face-centered cubic silver

crystals. These results indicate that crystalline silver nanoparticles were produced by plasma treatment of AgNO_3 -TSC-DW.

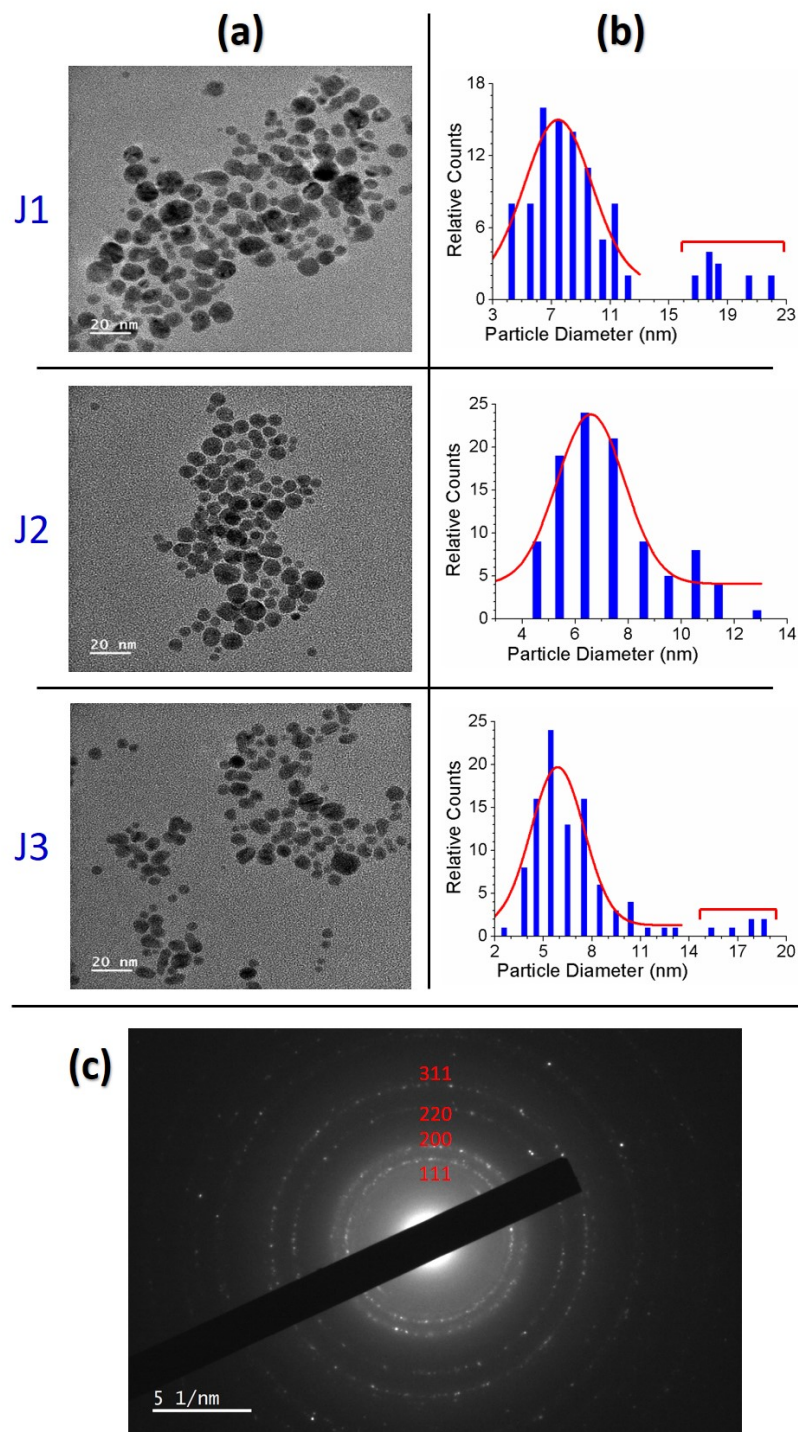
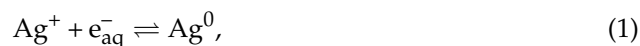


Figure 9. (a) HR-TEM images and (b) particle size distributions of the Ag@Cit NPs synthesized by treating AgNO_3 -TSC-DW for 10 min with the J1, J2, and J3 jets. (c) Electron diffraction patterns of the Ag@Cit NPs synthesized with the J2 jet.

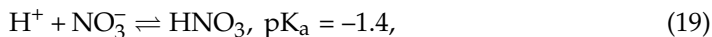
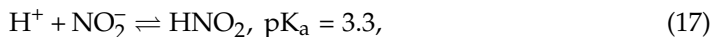
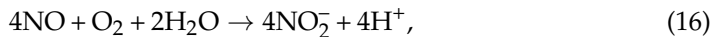
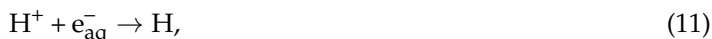
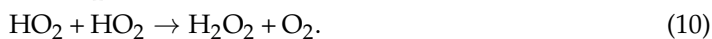
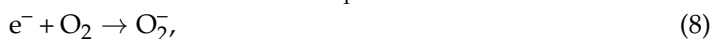
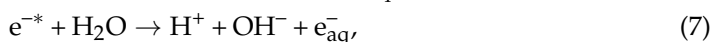
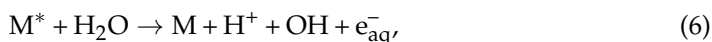
3.4. Plasma Synthesis Routes of Silver Nanoparticles

The plasma reduction routes of silver ion (Ag^+) to zero-valent silver (Ag^0) nanoparticles are well established, and are based on the two following reactions [5,23,43]:



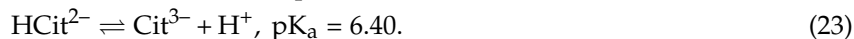
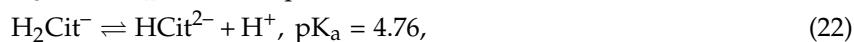
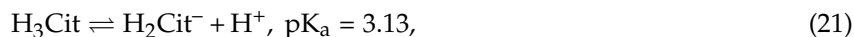
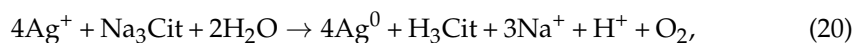
The reaction in Equation (1) is the reduction of silver ions by plasma electrons that are solvated into the aqueous solution. The main source of plasma electrons to reduce silver ions to *AgNPs* is the excited argon atoms. Plasma-excited argon atoms can provide plasma electrons that are required to reduce silver ions to *AgNPs*. The standard reduction potential of the silver ion is 0.80 V, which can instantly capture plasma electrons to form *AgNPs*. Equation (2) shows the reduction of silver ions through hydrogen atoms formed in the aqueous solution due to plasma–liquid interactions. Meanwhile, a large amount of hydrogen ions can digest silver nanoparticles (Equation (2)), leading to a smaller amount of *AgNPs*, as shown in Figure 8d.

Plasma consists of charged particles (electrons and ions), neutral particles, and UV light. When the plasma jet enters the aqueous solution, plasma radicals in gas phase can be transported to solution, and these solvated reactive species change the physicochemical properties of plasma-treated water. In the plasma-treated-DW and AgNO_3 -TSC-DW, additional reactive species can be generated through the following plasma–liquid interactions [44–49]:

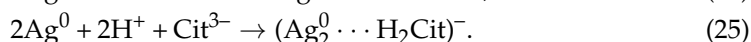
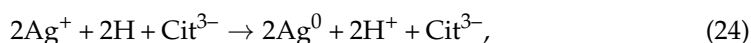


Here, e and e^-_{aq} are dry (non-hydrated) and aqua (hydrated) electrons, respectively, and M^* is any plasma ion with an ionization energy above the H_2O ionization threshold. In the plasma-treated DW, hydrogen ions were generated through plasma-induced UV photolysis (Equation (6)), and/or electrolysis (Equation (7)) of water molecules, and then the formation of the nitrate (nitrite)–hydrogen ion complex results in acidic water (Equations (17) and (19)), as shown in Figure 7a. For plasma treatment of the TSC-DW, plasma-generated hydrogen ions were captured by citrate (Figure 7c). Similarly to the plasma-treated TSC-DW, the plasma-treated AgNO_3 -TSC-DW exhibited higher pH values (Figure 7b).

Now we demonstrate the effects of citrate on the silver nanoparticle synthesis. Under higher pH conditions, *Ag@Cit NPs* can be efficiently synthesized from AgNO_3 and TSC ($\text{Na}_3\text{C}_6\text{H}_5\text{O}_7 = \text{Na}_3\text{Cit}$) [50,51]:



Here, $\text{Cit}^{3-} = (\text{C}_6\text{H}_5\text{O}_7)^{3-}$ is the citrate trianion. Citric acid ($\text{C}_6\text{H}_8\text{O}_7 = \text{H}_3\text{Cit}$) can be oxidized to citrate, and the oxidation products of citric acid depend on pH [52]. Under neutral or basic conditions ($6 \leq \text{pH} \leq 11$), the dominant structure of oxidized citric acid is a citrate trianion ($\text{C}_6\text{H}_5\text{O}_7 = \text{Cit}^{3-}$). In the plasma-treated AgNO_3 -TSC-DW, plasma-generated aqua electrons convert hydrogen ions to hydrogen atoms (Equation (11)). Hydrogen-induced reduction of silver ions is the dominant process for the plasma synthesis of *Ag@Cit NPs* because the reduction potential of the hydrogen ion is lower than that of the silver ion. In the plasma-treated AgNO_3 -TSC-DW, silver nanoparticles were produced from the reduction of silver ions through hydrogen atoms, and then a silver nanoparticle–citrate complex (*Ag@Cit NPs*) was formed [13].



Next, we consider the effects of plasma plume length on the plasma-synthesized silver nanoparticles. Experimentally, plasma treatment of the AgNO_3 -DW did not produce a sufficient amount of silver nanoparticles, whereas that of AgNO_3 -TSC-DW did. These results indicate that plasma electron-induced reduction of silver ions by reaction Equation (1) is not main synthesis route of silver nanoparticles under our experimental conditions. Next, citrate reduction of AgNO_3 -TSC-DW without boiling or plasma treatment failed to produce a sufficient amount of silver nanoparticles. Significant amounts of silver nanoparticles could be synthesized only when the plasma jet was applied to AgNO_3 -TSC-DW. Plasma-assisted citrate reduction of silver ions is more effective than citrate reduction of silver ions without plasma. Considering that reduction of silver ions by plasma electrons in the AgNO_3 -DW did not produce a sufficient amount of silver nanoparticles, the reduction of silver ions in AgNO_3 -TSC-DW is attributed to hydrogen atoms from the citrate (Equations (11) and (20)–(23)). In the plasma-treated AgNO_3 -TSC-DW, hydrogen-induced reduction of silver ions is the main synthesis route of silver nanoparticles. Efficient synthesis of silver nanoparticles can be achieved by citrate reduction of silver salt under neutral or basic conditions ($6 \leq \text{pH} \leq 11$) (Equations (21)–(25)) [51,53]. The synergetic effect between citrate and plasma electrons plays an important role in the plasma-synthesis of silver nanoparticles. The amount of plasma-synthesized *Ag@Cit NPs* was determined by the hydrogen atoms that were produced from the plasma electron-induced reduction of hydrogen ions. As shown in Figure 8c, longer-duration plasma treatment produced a larger amount of *Ag@Cit NPs*, because prolonged plasma treatment of AgNO_3 -TSC-DW led to more plasma electrons to be used for synthesis of *Ag@Cit NPs*. Regarding the effect of plasma plume length on the synthesis of silver nanoparticles, the amount of plasma-synthesized *Ag@Cit NPs* was largest in the J2 jet (Figure 8a). As shown in Figure 5b, the electrical conductivity was higher in the longer jets than in the J1 jet. The electrical conductivity of the J2 jet was significantly higher than that of the J1 jet, and the electrical conductivity of the J3 jet was slightly higher than that of the J2 jet. The longer jet produced higher electrical conductivity, indicating that more plasma electrons were generated in the longer jet (Figure 6). Meanwhile, the pH value of the J2 jet was higher than those of the shorter and longer jets, as shown in Figure 7b. That is, the J2 jet led to the highest pH value of the AgNO_3 -TSC-DW.

To further study the effect of plasma plume length on the synthesis of Ag@Cit NPs, we consider the relationship between the amount of plasma-synthesized silver nanoparticles and the acidity of the plasma-treated medium. From the silver nanoparticle synthesis reaction (Equation (2)) for reduction of silver ions through hydrogen atoms,

$$\frac{[\text{Ag}^0][\text{H}^+]}{[\text{Ag}^+][\text{H}]} = K_{\text{eq}}, \text{ at equilibrium.} \quad (26)$$

Here, K_{eq} is the equilibrium constant of the reaction (Equation (2)) for silver nanoparticle synthesis. $[\text{Ag}^0]$ and $[\text{Ag}^+]$ are the concentrations of zero-valent silver nanoparticles and silver ions, respectively. $[\text{H}^+]$ and $[\text{H}]$ are the concentrations of hydrogen ions and hydrogen atoms, respectively. At a fixed concentration of silver ions, a higher hydrogen atom concentration can produce a higher silver nanoparticle concentration, but a higher hydrogen ion concentration can digest silver nanoparticles. In the J1 and J3 jets, a lower pH indicates a larger number of hydrogen ions, which can convert AgNPs to silver ions, leading to a smaller number of Ag@Cit NPs. To summarize, the largest amount of Ag@Cit NPs obtained in the J2 jet is attributed to a higher pH and a larger number of aqua electrons. Plasma-assisted citrate reduction of silver ions is the main synthesis route of Ag@Cit NPs. In addition, citrate facilitates the conversion of silver ions to Ag@Cit NPs and stabilizes Ag@Cit NPs in an aqueous solution. Plasma-synthesized Ag@Cit NPs are well-dispersed in an aqueous solution. The formation of stabilized nanoparticles is due to electrostatic repulsion of citrate-capped AgNPs, as confirmed by the zeta potential of -55 mV.

3.5. Degradation Activity of Methylene Blue Dye Treated by Plasma-Synthesized Silver Nanoparticles

To confirm potential applications of the Ag@Cit NPs for the degradation of environmental pollutants, we investigated the degradation activity of plasma-synthesized Ag@Cit NPs on MB dye. The degradation activity of Ag@Cit NP treatment on MB was measured by optical absorption spectroscopy [54]. Figure 10a exhibits the absorption spectra of Ag@Cit NP-treated and -untreated MB solutions. The corresponding photos of Ag@Cit NP-treated MB solutions are displayed in Figure 10c. The pristine MB solution exhibited a broad absorption band with a strong peak at 670 nm and a shoulder at 615 nm [55]. The 670 nm absorption can be assigned to the MB monomer, and the 615 nm absorption can be attributed to the MB dimer. Comparing the Ag@Cit NP-treated MB with the pristine MB, the 670 nm absorption peak of MB disappeared by the Ag@Cit NP treatment. However, the Ag@Cit NP-treated MB exhibited significant absorption at 670 nm. To confirm the degradation activity of Ag@Cit NPs on MB, we measured the degradation activity of the nanoparticle-free plasma-activated medium (PAM). As positive controls of the plasma-synthesized Ag@Cit NPs, the TSC-DW solutions were treated with the J1, J2, and J3 jets for 10 min. As shown in Figure 10b, the 670 nm absorption intensity of PAM-treated-MB was similar to that of pristine MB, indicating that the degradation activity of Ag@Cit NPs is stronger than that of PAM. The nonzero absorption of Ag@Cit NP-treated MB at 670 nm may be ascribed to dye degradation products induced from the interaction of MB with Ag@Cit NPs. One possible explanation for the formation of dye degradation products by the Ag@Cit NP treatment is AgNP-induced electron transfer from BH_4^- ions to MB dye [56]. To fully understand the dye degradation mechanism by the Ag@Cit NP treatment, it will be necessary to conduct a more detailed study for exploring the dye degradation performance of Ag@Cit NPs and plasma-activated medium.

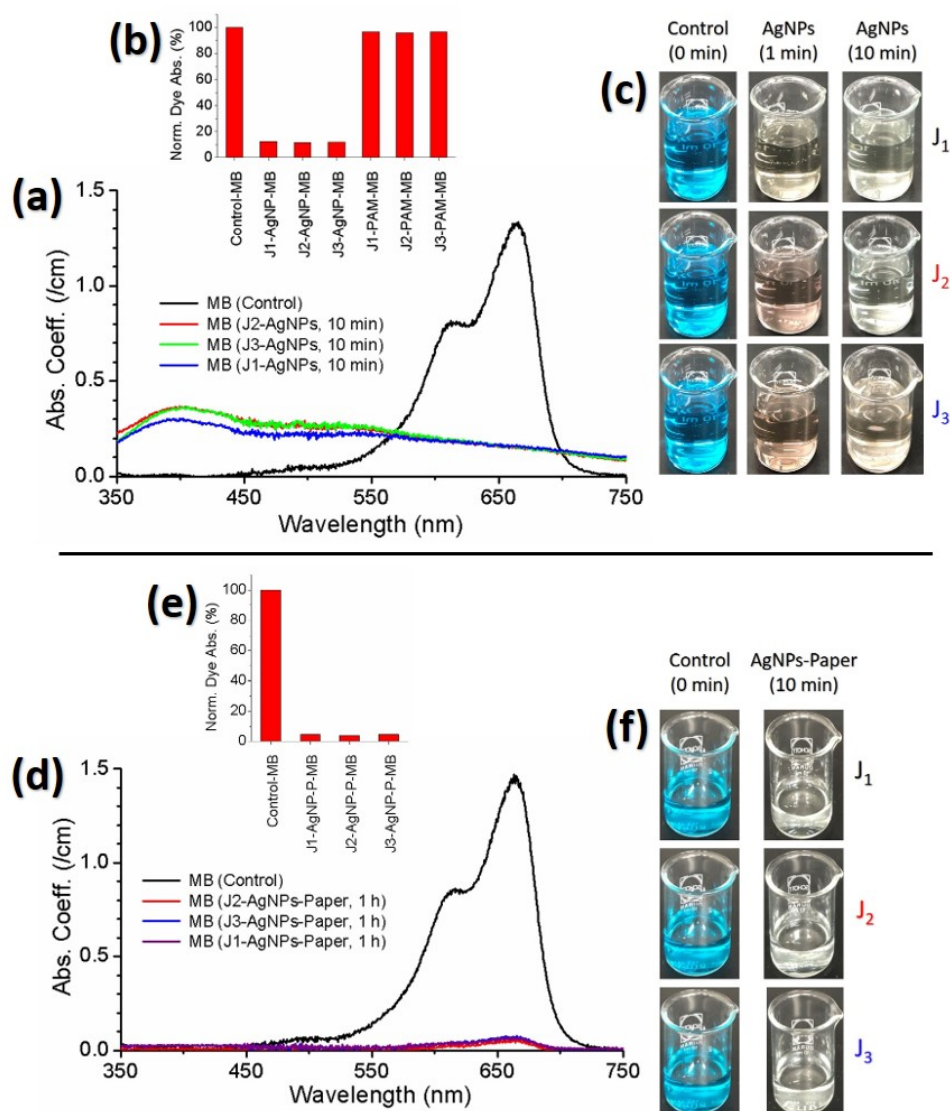


Figure 10. (a) Absorption spectra of Ag@Cit NP-treated MB solutions. (b) Dye degradation effects of Ag@Cit NPs and plasma-activated media (PAM). (c) Photos of Ag@Cit NP-treated MB. (d) Absorption spectra of Ag@Cit NP-paper-treated MB solutions. (e) Dye degradation effects of Ag@Cit NP-paper. (f) Photos of Ag@Cit NP-paper-treated MB. Ag@Cit NPs were synthesized by treating AgNO₃-TSC-DW for 10 min with the J1, J2, and J3 jets. Nanoparticle-free plasma-activated media were prepared by treating TSC-DW for 10 min with the J1, J2, and J3 jets. Solutions with 26 μ M MB were treated by plasma-synthesized Ag@Cit NPs.

Figure 10d exhibits the absorption spectra of Ag@Cit NP-paper-treated MB solutions. The corresponding photos of Ag@Cit NP-paper-treated MB solutions are displayed in Figure 10f. Comparing the 670 nm absorption peak of Ag@Cit NP-paper-treated MB with that of pristine MB, the 670 nm absorption peak of Ag@Cit NP-paper-treated MB decreased to almost zero, as shown in Figure 10e. Absorption spectra of the Ag@Cit NP-paper-treated MB solutions do not have an SPR absorption band of Ag@Cit NPs, indicating that degradation of MB dye without remnant silver nanoparticles was achieved by the Ag@Cit NP-paper treatment.

4. Conclusions

Citrate-capped silver nanoparticles were synthesized by treating AgNO₃-TSC-DW with atmospheric-pressure argon plasma jets. Ag@Cit NPs with an average particle diameter of about 5.9–7.5 nm were obtained after plasma treatment for 10 min. Plasma-

synthesized Ag@Cit NPs have a face-centered cubic structure, and their absorption spectra exhibited surface plasmon resonance peaks at approximately 406 nm. Citrate facilitated the conversion of silver ions to Ag@Cit NPs and stabilized AgNPs in an aqueous solution. Plasma-synthesized Ag@Cit NPs were well-dispersed in the aqueous solution. The amount of Ag@Cit NPs increased in a plasma-treatment duration-dependent manner. The acidity and electrical conductivity measurements showed that a larger amount of Ag@Cit NPs were produced from the 8.5 cm plume jet with a higher pH and a larger number of aqua electrons. Plasma synthesis of Ag@Cit NPs was more effective in the 8.5 cm plume jet than in the shorter and longer plume jets. These results indicate that the synergetic effect between plasma electrons and citrate played an important role in the plasma synthesis of Ag@Cit NPs. Plasma-synthesized Ag@Cit NPs exhibited significant dye degradation activity for methylene blue.

Author Contributions: G.J.L. conceived and performed the experiments, analyzed the data, and wrote the manuscript. T.R.A. performed the experiments and research, and wrote the manuscript. E.H.C. provided assistance in the plasma setup and the analysis of plasma-induced reactive oxygen and nitrogen species. All authors have read and agreed to the published version of the manuscript.

Funding: This research was supported by the Basic Science Research Program through the National Research Foundation of Korea funded by the Korean government (grant number NRF-2021R1A6A1A03038785, NRF-2018R1D1A1B07040386), and in part by Kwangwoon University in 2022.

Institutional Review Board Statement: Not applicable.

Informed Consent Statement: Not applicable.

Data Availability Statement: Not applicable.

Acknowledgments: Tirtha Raj Acharya acknowledges Pradeep Lamichhane for his technical assistance in the plasma experiment.

Conflicts of Interest: There are no conflicts of interest to declare.

References

1. Rycenga, M.; Cobley, C.M.; Zeng, J.; Li, W.; Moran, C.H.; Zhang, Q.; Qin, D.; Xia, Y. Controlling the synthesis and assembly of silver nanostructures for plasmonic applications. *Chem. Rev.* **2011**, *111*, 3669–3712. [[CrossRef](#)] [[PubMed](#)]
2. Garcia-Barrasa, J.; Lopez-de-Luzuriaga, J.M.; Monge, M. Silver nanoparticles: Synthesis through chemical methods in solution and biomedical applications. *Cent. Eur. J. Chem.* **2011**, *13*, 7–19. [[CrossRef](#)]
3. Lee, G.J.; Kang, M.; Kim, Y.; Choi, E.H.; Cho, M.J.; Choi, D.H. Optical assessment of chiral–achiral polymer blends based on surface plasmon resonance effects of gold nanoparticles. *J. Phys. D Appl. Phys.* **2019**, *53*, 095102. [[CrossRef](#)]
4. Kibis, L.S.; Stadnichenko, A.I.; Pajetnov, E.M.; Koscheev, S.V.; Zaykovskii, V.I.; Boronin, A.I. The investigation of oxidized silver nanoparticles prepared by thermal evaporation and radio-frequency sputtering of metallic silver under oxygen. *Appl. Surf. Sci.* **2010**, *257*, 404–413. [[CrossRef](#)]
5. Kondeti, V.S.S.K.; Gangal, U.; Yatom, S.; Bruggeman, P.J. Ag⁺ reduction and silver nanoparticle synthesis at the plasma-liquid interface by an RF driven atmospheric pressure plasma jet: Mechanisms and the effect of surfactant. *J. Vac. Sci. Technol. A* **2017**, *35*, 6130. [[CrossRef](#)]
6. Zhang, Y.T.; Guo, Y.; Ma, T.C. Plasma catalytic synthesis of silver nanoparticles. *Chin. Phys. Lett.* **2011**, *28*, 105201. [[CrossRef](#)]
7. Lee, H.; Park, S.H.; Jung, S.C.; Yun, J.J.; Kim, S.J.; Kim, D.H. Preparation of nonaggregated silver nanoparticles by the liquid phase plasma reduction method. *J. Mater. Res.* **2013**, *28*, 1105–1110. [[CrossRef](#)]
8. Yin, H.; Yamamoto, T.; Wada, Y.; Yanagida, S. Large-scale and size-controlled synthesis of silver nanoparticles under microwave irradiation. *Mater. Chem. Phys.* **2004**, *83*, 66–70. [[CrossRef](#)]
9. Eisa, W.H.; Abdel-Moneam, Y.K.; Shaaban, Y.; Abdel-Fattah, A.A.; Abou Zeid, A.M. Gamma-irradiation assisted seeded growth of Ag nanoparticles within PVA matrix. *Mater. Chem. Phys.* **2011**, *128*, 109–113. [[CrossRef](#)]
10. Pingali, K.C.; Rockstraw, D.A.; Deng, S. Silver nanoparticles from ultrasonic spray pyrolysis of aqueous silver nitrate. *Aerosol Sci. Technol.* **2005**, *39*, 1010–1014. [[CrossRef](#)]
11. Kodu, M.; Berholts, A.; Kahro, T.; Avarmaa, T.; Kasikov, A.; Niilisk, A.; Alles, H.; Jaaniso, R. Highly sensitive NO₂ sensors by pulsed laser deposition on graphene. *Appl. Phys. Lett.* **2016**, *109*, 113108. [[CrossRef](#)]
12. Henglein, A.; Giersig, M. Formation of colloidal silver nanoparticles: Capping action of citrate. *J. Phys. Chem. B*, **1999**, *103*, 9533–9539. [[CrossRef](#)]

13. Pillai, Z.S.; Kamat, P.V. What factors control the size and shape of silver nanoparticles in the citrate ion reduction method. *J. Phys. Chem. B* **2004**, *108*, 945–951. [\[CrossRef\]](#)
14. Lee, P.C.; Meisel, D. Adsorption and surface-enhanced Raman of dyes on silver and gold sols. *J. Phys. Chem.* **1982**, *86*, 3391–3395. [\[CrossRef\]](#)
15. Rodriguez-Sanchez, L.; Blanco, M.C.; Lopez-Quintela, M.A. Electrochemical synthesis of silver nanoparticles. *J. Phys. Chem. B* **2000**, *104*, 9683–9688. [\[CrossRef\]](#)
16. Habib, T.; Caiut, J.M.A.; Caillier, B. Synthesis of silver nanoparticles by atmospheric pressure plasma jet. *Nanotechnology* **2022**, *33*, 325603. [\[CrossRef\]](#)
17. Skiba, M.I.; Vorobyova, V.I.; Kosogina, I.V. Preparation of silver nanoparticles in a plasma-liquid system in the presence of PVA: Antimicrobial, catalytic, and sensing properties. *J. Chem.* **2020**, *2020*, 5380950. [\[CrossRef\]](#)
18. Mathew, T.V.; Kuriakose, S. Studies on the antimicrobial properties of colloidal silver nanoparticles stabilized by bovine serum albumin. *Colloid. Surface. B* **2013**, *101*, 14–18. [\[CrossRef\]](#) [\[PubMed\]](#)
19. Davoodbasha, M.; Lee, S.Y.; Kim, S.C.; Kim, J.W. One-step synthesis of cellulose/silver nanobiocomposites using a solution plasma process and characterization of their broad spectrum antimicrobial efficacy. *RSC Adv.* **2015**, *5*, 35052–35060. [\[CrossRef\]](#)
20. Nguyen, L.N.; Lamichhane, P.; Choi, E.H.; Lee, G.J. Structural and optical sensing properties of nonthermal atmospheric plasma-synthesized polyethylene glycol-functionalized gold nanoparticles. *Nanomaterials* **2021**, *11*, 1678. [\[CrossRef\]](#)
21. He, J.; Wen, X.; Wu, L.; Chen, H.; Hu, J.; Hou, X. Dielectric barrier discharge plasma for nanomaterials: Fabrication, modification and analytical applications. *TrAC Trend. Anal. Chem.* **2022**, *156*, 116715. [\[CrossRef\]](#)
22. Kaneko, T.; Baba, K.; Harada, T.; Hatakeyama, R. Novel gas-liquid interfacial plasmas for synthesis of metal nanoparticles. *Plasma Process. Polym.* **2009**, *6*, 713–718. [\[CrossRef\]](#)
23. Shirai, N.; Uchida, S.; Tochikubo, F. Synthesis of metal nanoparticles by dual plasma electrolysis using atmospheric dc glow discharge in contact with liquid. *Jpn. J. Appl. Phys.* **2014**, *53*, 046202. [\[CrossRef\]](#)
24. Reuter, S.; Von Woedtke, T.; Weltmann, K.D. The kINPen—A review on physics and chemistry of the atmospheric pressure plasma jet and its applications. *J. Phys. D Appl. Phys.* **2018**, *51*, 233001. [\[CrossRef\]](#)
25. Bruggeman, P.J.; Kushner, M.J.; Locke, B.R.; Gardeniers, J.G.; Graham, W.G.; Graves, D.B.; Hofman-Caris, R.C.; Maric, D.; Reid, J.P.; Ceriani, E.; et al. Plasma-liquid interactions: A review and roadmap. *Plasma Sources Sci. Technol.* **2016**, *25*, 053002. [\[CrossRef\]](#)
26. Bruggeman, P.J.; Frontiera, R.R.; Kortshagen, U.R.; Kushner, M.J.; Linic, S.; Schatz, G.C.; Andaraarachchi, H.; Exarhos, S.; Jones, L.O.; Mueller, C.M.; et al. Plasma-driven solution electrolysis. *J. Appl. Phys.* **2021**, *129*, 200902. [\[CrossRef\]](#)
27. Attri, P.; Kim, Y.H.; Park, D.H.; Park, J.H.; Hong, Y.J.; Uhm, H.S.; Kim, K.N.; Fridman, A.; Choi, E.H. Generation mechanism of hydroxyl radical species and its lifetime prediction during the plasma-initiated ultraviolet (UV) photolysis. *Sci. Rep.* **2015**, *5*, 9332. [\[CrossRef\]](#)
28. Lin, L.; Starostin, S.A.; Li, S.; Hessel, V. Synthesis of metallic nanoparticles by microplasma. *Phys. Sci. Rev.* **2018**, *3*, 200902.
29. Lamichhane, P.; Acharya, T.R.; Kaushik, N.; Nguyen, L.N.; Lim, J.S.; Hessel, V.; Kaushik, N.K.; Choi, E.H. Non-thermal argon plasma jets of various lengths for selective reactive oxygen and nitrogen species production. *J. Environ. Chem. Eng.* **2022**, *10*, 107782. [\[CrossRef\]](#)
30. Lamichhane, P.; Adhikari, B.C.; Nguyen, L.N.; Paneru, R.; Ghimire, B.; Mumtaz, S.; Lim, J.S.; Hong, Y.J.; Choi, E.H. Sustainable nitrogen fixation from synergistic effect of photo-electrochemical water splitting and atmospheric pressure N₂ plasma. *Plasma Sources Sci. Technol.* **2020**, *29*, 045026. [\[CrossRef\]](#)
31. Lu, X.; Naidis, G.V.; Laroussi, M.; Reuter, S.; Graves, D.B.; Ostrikov, K. Reactive species in non-equilibrium atmospheric-pressure plasmas: Generation, transport, and biological effects. *Phys. Rep.* **2016**, *630*, 1–84. [\[CrossRef\]](#)
32. Onishi, H.; Yamazaki, F.; Hakozaiki, Y.; Takemura, M.; Nezu, A.; Akatsuka, H. Measurement of electron temperature and density of atmospheric-pressure non-equilibrium argon plasma examined with optical emission spectroscopy. *Jpn. J. Appl. Phys.* **2021**, *60*, 026002. [\[CrossRef\]](#)
33. Lim, J.S.; Kim, R.H.; Hong, Y.J.; Lamichhane, P.; Adhikari, B.C.; Choi, J.; Choi, E.H. Interactions between atmospheric pressure plasma jet and deionized water surface. *Results Phys.* **2020**, *19*, 103569. [\[CrossRef\]](#)
34. Sornsakdanuphap, J.; Suanpoot, P.; Hong, Y.J.; Ghimire, B.; Cho, G.; Uhm, H.S.; Kim, D.; Kim, Y.J.; Choi, E.H. Electron temperature and density of non-thermal atmospheric pressure argon plasma jet by convective wave packet model. *J. Korean Phys. Soc.* **2017**, *70*, 979–989. [\[CrossRef\]](#)
35. Lee, G.J.; Sim, G.B.; Choi, E.H.; Kwon, Y.W.; Kim, J.Y.; Jang, S.; Kim, S.H. Optical and structural properties of plasma-treated *Cordyceps bassiana* spores as studied by circular dichroism, absorption, and fluorescence spectroscopy. *J. Appl. Phys.* **2015**, *117*, 023303. [\[CrossRef\]](#)
36. Ershov, A.; Borysov, J. Dynamics of OH ($X^2\Pi$, $v = 0$) in high-energy atmospheric pressure electrical pulsed discharge. *J. Phys. D Appl. Phys.* **1995**, *28*, 68–74. [\[CrossRef\]](#)
37. Rahman, A.; Yalin, A.P.; Surla, V.; Stan, O.; Hoshimiya, K.; Yu, Z.; Littlefield, E.; Collins, G.J. Absolute UV and VUV emission in the 110–400 nm region from 13.56 MHz driven hollow slot microplasmas operating in open air. *Plasma Sources Sci. Technol.* **2004**, *13*, 537–547. [\[CrossRef\]](#)
38. Lee, G.J.; Lamichhane, P.; Ahn, S.J.; Kim, S.H.; Yewale, M.A.; Choong, C.E.; Jang, M.; Choi, E.H. Nitrate capture investigation in plasma-activated water and its antifungal effect on *Cryptococcus pseudolongus* cells. *Int. J. Mol. Sci.* **2021**, *22*, 12773. [\[CrossRef\]](#)

39. Sarani, A.; Nikiforov, A.Y.; Leys, C. Atmospheric pressure plasma jet in Ar and Ar/H₂O mixtures: Optical emission spectroscopy and temperature measurements. *Phys. Plasma* **2010**, *17*, 063504. [[CrossRef](#)]
40. Rumbach, P.; Bartels, D.M.; Sankaran, R.M.; Go, D.B. The solvation of electrons by an atmospheric-pressure plasma. *Nat. Commun.* **2015**, *6*, 1–7. [[CrossRef](#)]
41. Siefermann, K.R.; Liu, Y.; Lugovoy, E.; Link, O.; Faubel, M.; Buck, U.; Winter, B.; Abel, B. Binding energies, lifetimes and implications of bulk and interface solvated electrons in water. *Nat. Chem.* **2010**, *13*, 274–279. [[CrossRef](#)]
42. Schmidt, K.H.; Buck, W.L. Mobility of the hydrated electron. *Science* **1966**, *151*, 70–71. [[CrossRef](#)] [[PubMed](#)]
43. Wu, H.; Liu, Z.; Xu, L.; Wang, X.; Chen, Q.; Ostrikov, K. The Ag⁺ reduction process in a plasma electrochemical system tuned by the pH value. *J. Electrochem. Soc.* **2021**, *168*, 123508. [[CrossRef](#)]
44. Schmidt-Bleker, A.; Winter, J.; Bosel, A.; Reuter, S.; Weltmann, K.D. On the plasma chemistry of a cold atmospheric argon plasma jet with shielding gas device. *Plasma Sources Sci. Technol.* **2015**, *25*, 015005. [[CrossRef](#)]
45. Schmidt-Bleker, A.; Winter, J.; Iseni, S.; Dunnbier, M.; Weltmann, K.D.; Reuter, S. Reactive species output of a plasma jet with a shielding gas device-combination of FTIR absorption spectroscopy and gas phase modelling. *J. Phys. D Appl. Phys.* **2014**, *47*, 145201. [[CrossRef](#)]
46. Lundberg, J.O.; Weitzberg, E.; Gladwin, M.T. The nitrate–nitrite–nitric oxide pathway in physiology and therapeutics. *Nat. Rev. Drug Discov.* **2008**, *7*, 156–167. [[CrossRef](#)]
47. Uhm, H.S. Generation of various radicals in nitrogen plasma and their behavior in media. *Phys. Plasmas* **2015**, *22*, 123506. [[CrossRef](#)]
48. Uhm, H.S.; Na, Y.H.; Lee, C.B.; Choi, E.H.; Cho, G. Dissociation and excitation coefficients of nitrogen molecules and radical generation in nitrogen plasma. *Curr. Appl. Phys.* **2014**, *14*, S162–S166. [[CrossRef](#)]
49. Yamasaki, H. Nitrite-dependent nitric oxide production pathway: Implications for involvement of active nitrogen species in photoinhibition in vivo. *Trans. R. Soc. Lond. B Biol. Sci.* **2000**, *355*, 1477–1488. [[CrossRef](#)]
50. Tan, K.S.; Cheong, K.Y. Advances of Ag, Cu, and Ag–Cu alloy nanoparticles synthesized via chemical reduction route. *J. Nanopart. Res.* **2013**, *15*, 1537. [[CrossRef](#)]
51. Marciniak, L.; Nowak, M.; Trojanowska, A.; Tylkowski, B.; Jastrzab, R. The effect of pH on the size of silver nanoparticles obtained in the reduction reaction with citric and malic acids. *Materials* **2020**, *13*, 5444. [[CrossRef](#)] [[PubMed](#)]
52. Goldberg, R.N.; Kishore, N.; Lennen, R.M. Thermodynamic quantities for the ionization reactions of buffers. *J. Phys. Chem. Ref. Data* **2002**, *31*, 231–370. [[CrossRef](#)]
53. Djokic, S. Synthesis and antimicrobial activity of silver citrate complexes. *Bioinorg. Chem. Appl.* **2008**, *2008*, 436458. [[CrossRef](#)] [[PubMed](#)]
54. Naaz, F.; Farooq, U.; Khan, M.M.; Ahmad, T. Multifunctional efficacy of environmentally benign silver nanospheres for organic transformation, photocatalysis, and water remediation. *ACS Omega* **2020**, *13*, 26063–26076. [[CrossRef](#)]
55. Shahinyan, G.A.; Amirbekyan, A.Y.; Markarian, S.A. Photophysical properties of methylene blue in water and in aqueous solutions of dimethylsulfoxide. *Spectrochim. Acta A* **2019**, *217*, 170–175. [[CrossRef](#)]
56. Jana, N.R.; Sau, T.K.; Pal, T. Growing small silver particle as redox catalyst. *J. Phys. Chem. B* **1999**, *103*, 115–121. [[CrossRef](#)]